A Pragmatic Part Scale Model for Residual Stress and Distortion Prediction in Powder Bed Fusion

Richard J. Williams, Catrin M. Davies, Paul A. Hooper

Department of Mechanical Engineering, Imperial College London, SW7 2AZ, UK

Abstract

Parts manufactured by laser powder bed fusion contain significant residual stress. This stress causes failures during the build process, distorts parts and limits in-service performance. A pragmatic finite element model of the build process is introduced here to predict residual stress in a computationally efficient manner. The part is divided into coarse sections which activate at the melting temperature in an order that imitates the build process. Temperature and stress in the part are calculated using a sequentially coupled thermomechanical analysis with temperature dependent material properties. The model is validated against two sets of experimental measurements: the first from a bridge component made from 316L stainless steel and the second from a cuboidal component made from Inconel 718. For the bridge component the simulated distortion is within 5% of the experimental measurement when modelled with a section height of 0.8 mm. This is 16 times larger than the 50 μm layer height in the experimental part. For the cuboid component the simulated distortion is within 10% of experimental measurement with a section height 10 times larger than the experiment layer height. These results show that simulation of every layer in the build process is not required to obtain accurate results, reducing computational effort and enabling the prediction of residual stress in larger components.

Keywords: residual stress prediction; powder bed fusion; distortion; process modelling; selective laser melting

1. Introduction

In powder bed fusion (PBF) a moving localised heat source melts metal powder to manufacture three dimensional components. Thermal gradients are created by the heat source and conduction through previously melted layers. The material expands and contracts as it is thermally cycled and this leads to residual stress. The residual stress can cause geometric distortion, resulting in the scrappage of parts if they are outside dimensional tolerances. In extreme cases cracking and other failures can occur during the build process itself [1]. In-service performance of a component is also often compromised by the presence of residual stress.

Email address: paul.hooper@imperial.ac.uk (Paul A. Hooper)

Current approaches to minimise residual stress are to carry out a post-process stress relief heat treatment or hot isostatic pressing (HIP). Several iterations of the part design and optimisation of the manufacturing processing parameters are often required to achieve satisfactory results. All of this is costly and time consuming. Tools to predict these stresses accurately and quickly are needed before the adoption of PBF processes in safety critical industries [2]. Finite element (FE) modelling of the process provides a tool to predict these stresses and distortions. This information can then be used to optimise component design and manufacture both quickly and cost effectively.

Existing models of PBF processes can largely be categorised into micro and macro scale models [3]. Micro scale models focus on the heat source interaction zone and are useful for understanding stability of the melt pool and defect formation. Capturing all of the melt pool process physics across an entire build is not feasible with contemporary computing resources. Macro scale models are of interest when investigating residual stress as these focus on a part sized length scale. Most existing macro scale models ignore many of the complex mechanisms related to the melt pool and consolidation. The laser input energy is simulated as a moving heat source with the same length scale as the focused laser spot. Temperature and mechanical stresses are then calculated from a coupled thermomechanical analysis [4, 5, 6, 7, 8, 9, 10, 11]. Even with these simplifications it is not feasible to simulate larger components in a useful time frame.

The thermal energy input has frequently been captured by computing the movement of a surface or volumetric heat flux. A 2D Gaussian shaped flux profile has been used extensively [7, 8, 12]. The Goldak heat source model has also been used by many authors as it accounts for penetration depth [4, 13]. One issue with modelling the PBF heat source at its true size, in the order of 50 to 100 μm, is the vast disparity in length scale relative to the total path distance scanned by the laser. Consequently, a large number of calculations are required even for just a single layer. This has restricted many models to a few scan tracks or layers.

Studies in the literature have focussed on the more widely used materials: 316L stainless steel, Ti-6Al-4V and Inconel alloys. Many authors have opted to resolve the change in physical state and describe temperature dependent mechanical properties of the material. Several authors have developed models for the material in the bulk solid, liquid and powdered state. They use a sub-routine to call on the temperature and determine which of the material models should be applied [4, 6, 14]. Whilst this is the truest representation of the process physics, the complexity of using multiple material models has again proven restrictive in terms of computational expense. Simplifications can be made by neglecting changes in state [15] and omitting temperature dependency of the material properties [11]. Contuzzi et al. reported validation against melt pool depth and track widths observed via micrograph to a variation of under 10% [11]. This is a comparable level of accuracy to that in [4], which used a far more sophisticated material model, demonstrating that simplifications can be made whilst still maintaining accuracy.

The additive nature of the process has commonly been modelled by activating sections of the geometry using the element birth technique widely available in commercial FE packages. Various schemes of activation have been investigated, with some authors activating small sections of geometry at a time and others smearing the deposition to a whole layer or several layers at a time. Many authors activate a whole layer at a time before scanning the heat source over it and this is the most common approach [8, 11, 12]. There may be opportunities for further coarsening of the deposition method whilst still

retaining suitable accuracy for stress and net shape prediction, as demonstrated by [16]. A further limitation of depositing the material layer-wise is the greater number of steps required in the analysis and complexity of the model mesh. This has again been a reason for many of the models cited consisting of only a few layers.

Some basic studies correlating experimental track widths to the size of the melt pool in the thermal model have been used to validate thermal models [4, 8, 17]. Other authors have relied on validation against third party data [12, 18], but often no validation work is presented at all. Most of the studies identified have modelled a part domain of only a few millimetres in size, containing single tracks or layers. Modelling parts of a greater size makes it easier to measure distorted shapes after sectioning from the build plate, allowing the mechanical analysis in the model to be validated. This approach was used by Hodge et al. in [19] and Kruth et al. in [20], however this naturally adds to the computation time as larger part domains are analysed.

This paper presents a pragmatic approach to the computational modelling of the PBF process, allowing the prediction of residual stress across a realistic workpiece geometry. The model is described as pragmatic as it is computationally efficient, captures only what is necessary to solve the problem and is easy to apply to real world problems. A 316L stainless steel bridge component and an Inconel 718 cuboidal component are simulated and validated against experimental measurements. The paper is structured as follows. A generalised description of the modelling approach is given first. This is then followed by modelling details specific to each geometry. Experimental methods used to measure the distortions of the 316L component are then detailed along with the methods used by [21] to measure the distortion of the Inconel 718 component. Results for each simulation and experiment are then compared and discussed before conclusions are drawn about the benefits of the pragmatic modelling approach.

2. Powder bed fusion modelling strategy

Thermally induced residual stresses are developed due to the generation of steep temperature gradients in a material. Thermal expansion and contraction of the material is accommodated by elastic and plastic deformation. Residual stress is the stress that remains when the thermal gradient is removed and the material reaches an equilibrium temperature. In PBF, a localised and fast moving heat source provides thermal energy input to the system and produces a melt pool. The temperature range in the melt pool region is transient and above the range relevant for residual stress development. It is therefore possible to simplify the prediction of residual stress by neglecting the melt pool at its true length scale, allowing coarser meshes and larger time steps to be used without sacrificing accuracy.

The model was implemented using the commercially available FE software ABAQUS [22]. In this section common attributes of the implemented model are described first, followed by two specific geometries that have been modelled and experimentally verified.

2.1. Deposition methodology

Additively manufactured components are comprised of many layers. In PBF these layers are often 50 μm in height. The approach of the model is to amalgamate several of these layers into a thicker section or block. This is built upon the 'block dump'

approach previously used in weld modelling to achieve accurate simulation at reduced computational expense [23]. The sections are then activated sequentially throughout the analysis using the element birth and death technique (or the *MODELCHANGE facility within ABAQUS). Initially they are all present and then they are all removed in an initial step, before being reactivated again block-by-block. This represents the additive nature of the process. The number and size of the blocks in the model is varied to establish a limit in the layer coarsening up to which accuracy of results is maintained.

In the interest of computational efficiency, a sequentially coupled thermomechanical analysis is used. The thermal analysis first resolves the transient temperature field across the part. The nodal temperatures at the corresponding time step are then read into the mechanical model to evaluate the stress caused by thermal expansion.

2.2. Thermal analysis

The thermal analysis is governed by the transient heat conduction equation:

$$\rho c_p \frac{\partial T}{\partial t} - \nabla \cdot (k \nabla T) = 0 \tag{1}$$

where ρ is the density, c_p is the specific heat capacity, T is the temperature, t is time and k is thermal conductivity. Eight node linear diffusive heat transfer brick elements (DC3D8) elements are employed in the thermal analyses. Each block is reactivated in turn at the melting temperature. This captures the cyclic heating and cooling nature of the process, albeit the heat input is scaled up across a far larger volume than the true melt pool size. Significant computational savings are also made using this method as the model does not have to solve the thermal field as the laser heat source moves across the layer, allowing longer time steps in the computational procedure. The thermal boundary conditions used for each component modelled are described in sections 3 and 4.

2.3. Mechanical analysis

The nodal temperatures are imported into the mechanical analysis at each time step and stress and distortion are evaluated according to the material model. The mechanical analysis is governed by the equilibrium equation 2 and stress, σ, is evaluated by equation 3 where C is the stiffness tensor and ε_e, ε_p and ε_T are the elastic, plastic and thermal strain components respectively. The thermal strain component driving the residual stress is calculated according to equation 4 [24] where α is the coefficient of thermal expansion and ΔT is the change in temperature.

$$\nabla \cdot \sigma = 0 \tag{2}$$

$$\sigma = C\varepsilon = C(\varepsilon_e + \varepsilon_p + \varepsilon_T) \tag{3}$$

$$\varepsilon_T = \alpha \cdot \Delta T \tag{4}$$

A detailed description of the continuum mechanics and heat transfer related to the problem is presented in [25].

The analysis steps in the mechanical model follow those in the thermal model, using the same *MODELCHANGE interactions to reactivate the geometry block-by-block

whilst the part has fixed boundary conditions. The mechanical boundary conditions employed for each component modelled are described below.

A temperature dependent elastic-plastic material model is used. Temperature dependent conductivity, coefficient of thermal expansion and specific heat capacity are also included. An isotropic hardening model is used for simplicity. In the mechanical analysis continuum, eight node linear brick elements with reduced integration elements (C3D8R) are used. These are analogous to the heat transfer elements in the thermal analysis, allowing the meshes to be compatible. Reduced integration elements are used to enhance computational efficiency.

3. Bridge component model

The bridge geometry modelled here is similar to that experimentally examined by Kruth et al. [20]. The model geometry and mesh employed are shown in Figure 1. The mesh contains 145,908 elements with an average volume of $0.22 \times 0.37 \times 0.21\,\text{mm}$ in xyz respectively, as defined in Figure 1. A mesh convergence study confirmed the solution is mesh independent at this element size. The geometry is divided into blocks in both the x and z coordinate directions, with each block consisting of a number of elements. A schematic depicting the block divisions are shown in Figure 2. In this example six vertical block divisions and two horizontal block divisions are made, corresponding to a block height 1.67 mm and maximum width of 20 mm (in the top section of the bridge). The blocks are deposited sequentially in the order corresponding to the number labelled on the block.

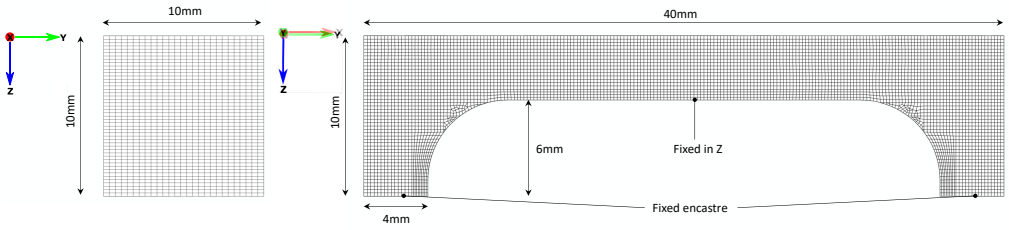

Figure 1: Geometry and mesh of the bridge component.

3.1. Thermal parameters

As the melt pool and associated phenomena are not considered in this analysis, conduction is the dominant mode of heat transfer in the part. In addition to the thermal analysis principles described in Section 2.2, conduction into the base plate is modelled using an artificially high heat convection boundary condition. This eliminates the need to explicitly model the base plate. An equivalent convective heat transfer coefficient of $1250\,\text{W/mK}$ is estimated based upon the known conductivity of bulk 316L. For the underside surface of the bridge (where build support structures would be present) the same boundary condition is applied but the heat transfer coefficient is reduced to 30% of the value for the base. This is to reflect the lower density over which supports cover the part surface.

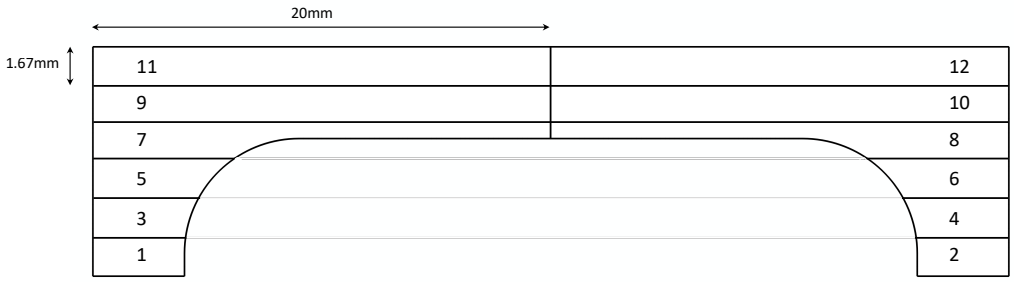

Figure 2: 2D schematic of the bridge component showing an example of a model containing six vertical block divisions and two horizontal divisions. The numbers indicate the order in which the blocks are deposited.

As the melt pool and associated phenomena are not considered in this analysis, conduction is the dominant mode of heat transfer in the part. Several iterations of the model revealed that including convection or radiation heat loss or conduction through the surrounding powder has a negligible impact on results and thus these other modes of heat transfer are neglected. The procedure of the thermal analysis is shown in Figure 3, demonstrating the sequential deposition of the blocks and the transient temperature profile changing throughout. In this example there are 12 blocks in the vertical (z) direction and 8 block divisions in the horizontal (x) direction, corresponding to a block height of 0.83 mm and a maximum block width of 5 mm occurring in the upper section of the bridge.

This model scenario is used to investigate the effects of varying block dimensions in both the x and z directions, as defined in Figure 1. This causes the transient thermal field in the model to be different in each case and also impacts the structural analysis. The aim is to identify the block size at which results converge and no benefit is gained from further refinement.

3.2. Mechanical boundary conditions

The part is built-in on the bottom surface of each side of the bridge, representing it being fused directly the baseplate. Additionally, the surfaces where supports are located are fixed in the z direction. This replicates the effect of the supports, anchoring the part and allowing the overhang to be built. In the final analysis step, the fixed condition is removed from the supports and the displacement boundary condition is removed from one side of the bridge, leaving it built in only at one end. This is equivalent to the wire Electrical Discharge Machining (EDM) cut used in the experiment and allows the part to deform and partly relieve the stress field.

In general AM material has been found to have significantly higher yield strength than wrought material at room temperature [26, 27, 28]. Limited testing has been performed to describe the tensile behaviour of PBF material at a range of temperatures. A Johnson-Cook plasticity model [29] is therefore used (neglecting strain rate effects) to describe the plastic flow stress, σ_{y}, in terms of the equivalent plastic strain, ε_{p}, and is given as:

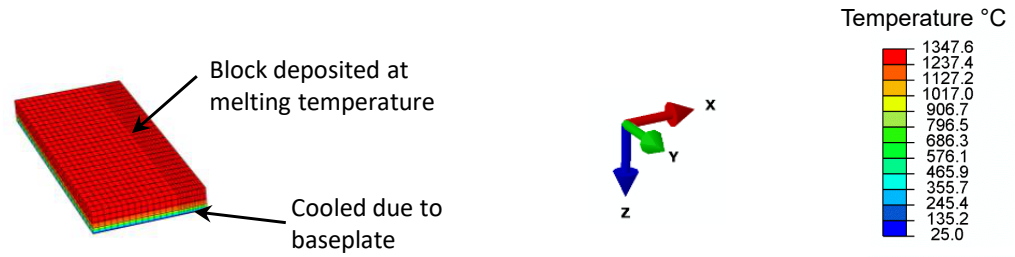

(a)

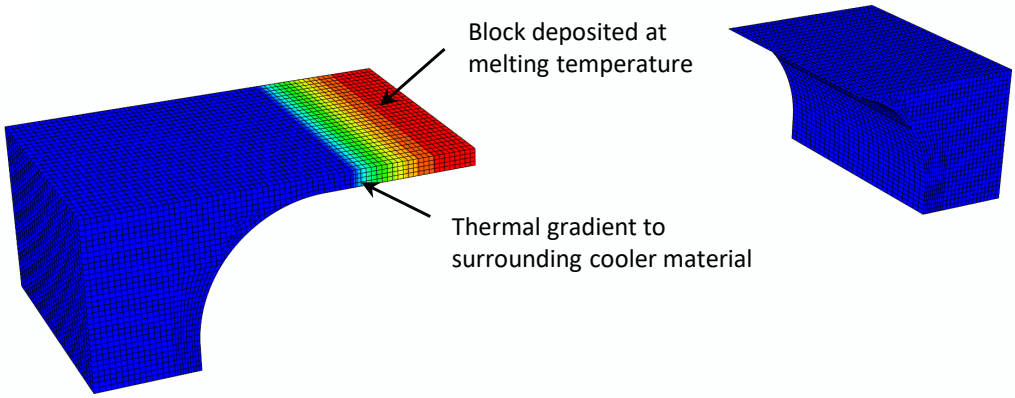

(b)

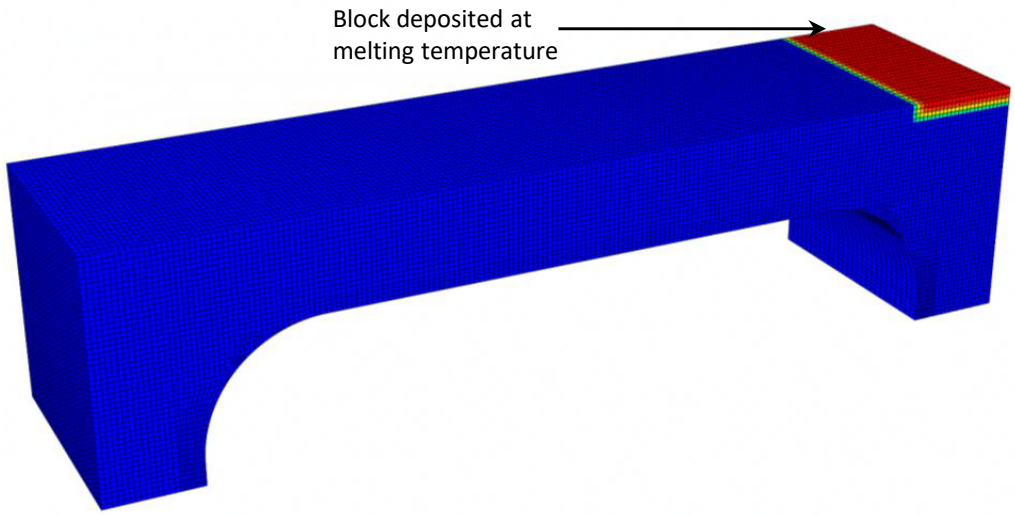

(c)

Figure 3: Sequence showing evolving temperature field in the bridge component as blocks are reactivated in the model for the (a) 1^{st} block, (b) 17^{th} block and (c) final (54^{th}) block. In this case there are 12 vertical (z) block divisions and eight horizontal block divisions (x).

$$\sigma_{\mathrm{y}} = \left(A + B\varepsilon_{\mathrm{p}}^{n}\right)\left(1 - \left(\frac{T - T_0}{T_{\mathrm{m}} - T_0}\right)^{m}\right) \tag{5}$$

The model is purely empirical and constants are found by fitting to experimental data. Parameter A is equivalent to the yield strength at the reference temperature T_0 and constants B and n describe the material hardening behaviour and were determined from the tensile test results found in [26, 27, 30]. Parameter m describes the temperature dependency and T_{m} is the melting temperature. Due to the absence of detailed temperature dependent tensile data for this AM material, the temperature dependency parameter m is assumed to be the same as that of the wrought material used in [31]. The values of the Johnson-Cook parameters used in the model are given in Table 1.

Table 1: Johnson-Cook constitutive plasticity model parameters used in the bridge model.

Parameter	Value
A	500 MPa
B	600 MPa
n	0.6155
m	1.042

4. Cuboidal component on thin substrate model

The second geometry is based upon work presented by Denlinger et al. [5], which was validated using an experimental setup devised by Dunbar et al. in [21]. The part consisted of a small 6.35×6.35 mm square cross section which was 1.5 mm thick. This was built on top of a larger 0.81 mm thick substrate that was supported at it ends. Both the part and substrate were manufactured from Inconel 718. The model presented in [5] simulated the laser beam at its true length scale and utilised advanced techniques such as adaptive mesh refinement in a bespoke solver optimised for modelling PDF. The pragmatic model presented here follows the same general modelling approach as previously described. The part is divided into four vertical blocks which are all initially deactivated then reintroduced at the melting temperature of Inconel 718 (approximately 1200 °C).

4.1. Thermal parameters

In this case block divisions are made in the z direction only, owing to the uniformity of the geometry. Four blocks were chosen in the final version of this model after carrying out a preliminary convergence investigation. This number gave sufficiently accurate results whilst maintaining maximum computational efficiency. The substrate is present throughout the analysis and the problem is modelled as a single monolithic part, avoiding the complexity of defining contact properties between two parts. A convection boundary condition is applied to all surfaces of the substrate to account for heat loss via all three modes of heat transfer and this value is determined to be 25 $\mathrm{W/mK}$ by the authors in [5] and [21]. Although convective heat transfer is deemed negligible for the case of the bridge part, it has a more significant effect in this case as the surface area to volume ratio is relatively large.

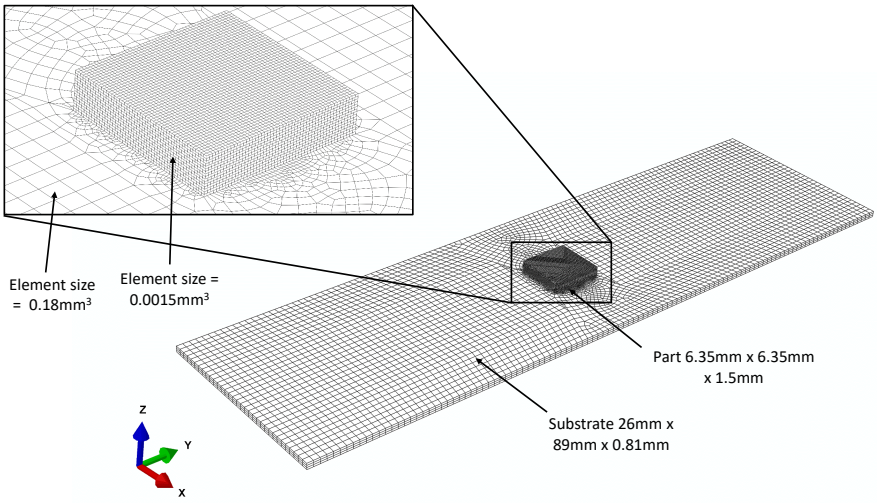

Figure 4: FE mesh used in the cuboid component model.

An image of the FE mesh is shown Figure 4. The part section of the mesh contains 40,000 elements with a typical volume of $0.0015\,\mathrm{mm}^3$ and the substrate contains 20,310 elements with a volume of $0.18\,\mathrm{mm}^3$. As with the bridge model, a mesh density convergence study found that these element sizes are sufficient.

4.2. Mechanical parameters

The mechanical boundary conditions are set to represent those in the experiment. The substrate is fixed at the locations of the bolts and pinned in the z direction where the support screws are located (shown in Figure 6). The temperature and displacement can then be extracted from the results at the nodes closest to the location of the instrumentation apparatus in the experiment. The material model used is based on the temperature dependent material property data published in [5]. This again neglects changes of phase and state and describes the temperature dependent thermomechanical properties of Inconel 718.

5. Experimental methods

5.1. Bridge component

The bridge component was manufactured from 316L stainless steel on a Renishaw AM250 machine to verify the distortion predicted by the part scale model. The process parameters used in the build are shown in Table 2. Upon completion, one side of the bridge was cut from the build plate by wire EDM, causing it to deflect upwards due to the stress profile present in the part. This is as per the analysis procedure in the FE model. This warping effect is typical when removing parts from the substrate post build and is also a common cause of build failures and out of tolerance net shape.

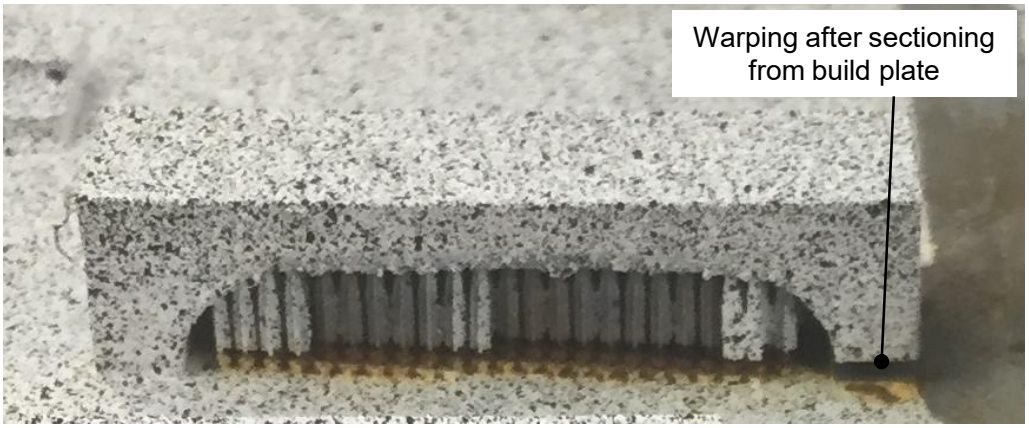

Figure 5: A bridge component made from 316L stainless steel on the build plate after speckling and sectioning on one side for DIC analysis.

Table 2: Build parameters used during the bridge manufacture.

Parameter	Value
Power	180 W
Exposure time	110 μs
Point distance	65 μm
Hatch distance	125 μm
Layer Height	50 μm
Scan Strategy	Chessboard [32]

3D digital image correlation (DIC) was used to measure the top surface profile of the bridge before and after being cut from the build plate. This enabled deflection to be calculated after the part had been cut away. An image of the bridge component after sectioning and DIC analysis is shown in Figure 5. The distortion can be seen in this image as the free side of the bridge has lifted upwards. The validation principle is based on work done in [20] and [33] and is a distortion measurement technique. However, the paper by Wu et al. [33] remarks that it is suitable for giving qualitative insight into process induced residual stress. It is well matched to this model, which predicts macro residual stresses which act across the length scale of the body and give rise to geometric distortion.

5.2. Cuboid component

The experimental set up from [21] can be seen in Figure 6. The part is shown in grey and was built upon a thin substrate that is shown in white. The thermal cycling and distortion of the part during and after processing were monitored by fitting the substrate with thermocouples and a linear variable differential transformer (LVDT). The LVDT was attached to the bottom surface in the location marked LVDT in Figure 6 to measure the out-of-plane displacement at the centre of the substrate.

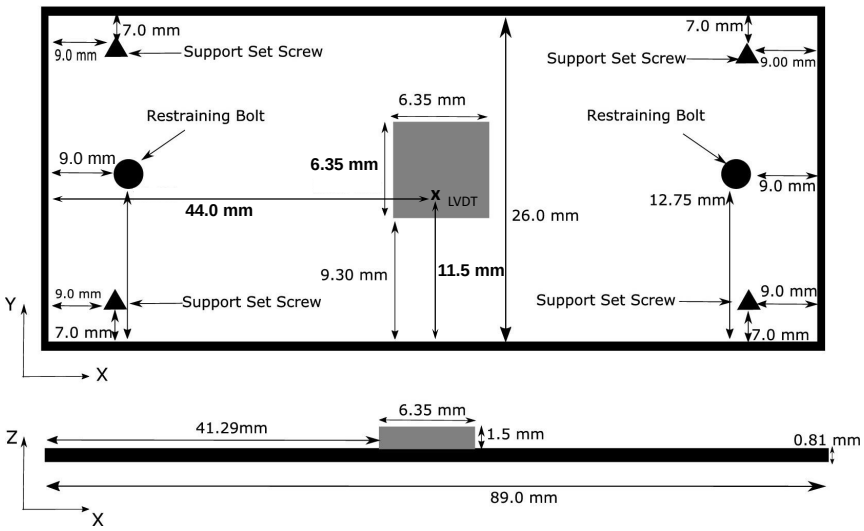

Figure 6: Schematic of experimental set up showing the component (in grey) and measurement substrate (figure adapted from [21]).

6. Simulation results and validation

6.1. Bridge component

The top surface vertical displacement profile measured by DIC is shown in Figure 7. The experimental bridges show a maximum vertical deflection of approximately 0.8 mm at the end from which the part was cut.

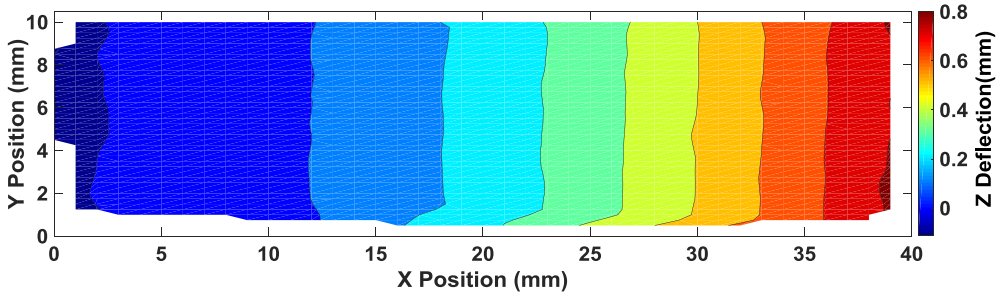

Figure 7: Plot showing the top surface displacement of the bridge after cutting as measured by DIC.

The effect of varying block height in the vertical direction is shown in Figure 8. The lines show the top surface vertical deflection along the y centreline of the part. The plot shows results of several vertical block heights which all contain two horizontal blocks per vertical layer. This corresponds to a block width of 20 mm in the top section of the bridge. The experimentally measured deflection is also shown.

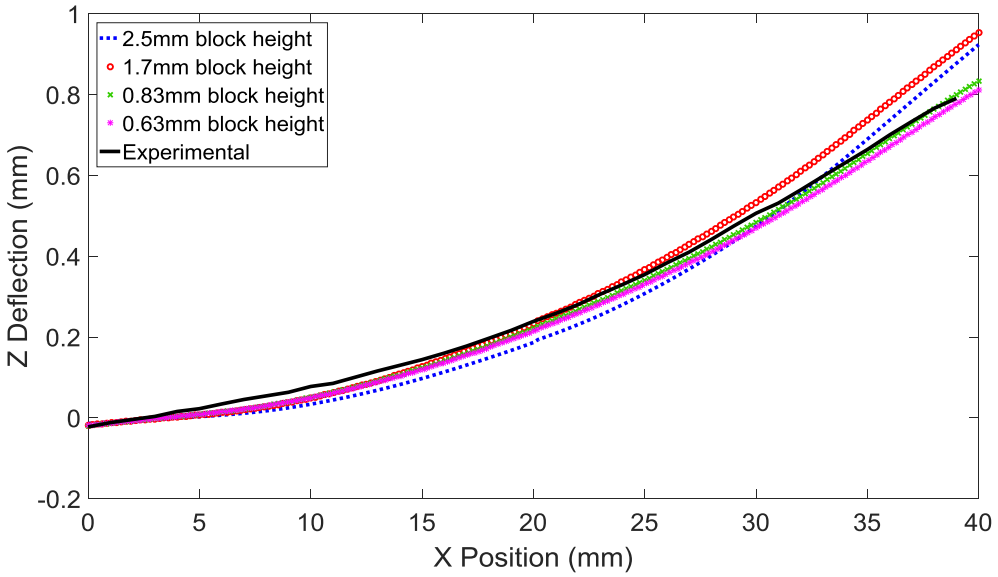

Figure 8: Plot showing the deflection in the z direction along the length in the x direction of the models with two horizontal blocks and varying block height in the z direction.

As the vertical block height in the simulation decreases the deflection of the top surface approaches that measured experimentally. It can also be seen that there is a small negative deflection on the left hand side of the bridge as it has rotated about the fixed end. For a block height of less than 0.83 mm agreement to within 5% of the experimental measurement can be seen. In this scenario this is the optimum modelled layer height in terms of speed and accuracy.

The effects of varying the number of blocks in the horizontal (x) direction are shown in Figure 9. Results from two models containing two and eight blocks in the horizontal direction are shown. This equates to a maximum block width of 20 mm and 5 mm in the upper section of the bridge respectively. Both models have a vertical block height of 0.83 mm.

The spread of results between the models with 5 mm block width and 20 mm block width is relatively low. As the fidelity of the model is increased the number of horizontal blocks becomes less important in influencing the results.

6.2. Cuboid component

For the cuboid component simulation the deflection has been extracted at the node corresponding to the location of the LVDT in the experiment in [21]. This allows comparison between the predicted distortion of the substrate and that measured experimentally using the LVDT. A plot of the deflection measured experimentally by Dunbar et al. and the node deflection in the pragmatic model is shown in Figure 10.

The underside of the substrate deflected vertically downwards along with the part, as measured by the LVDT. Although the pragmatic model does not capture the individual layer transients of the process, agreement to within 10% can be seen with the longer

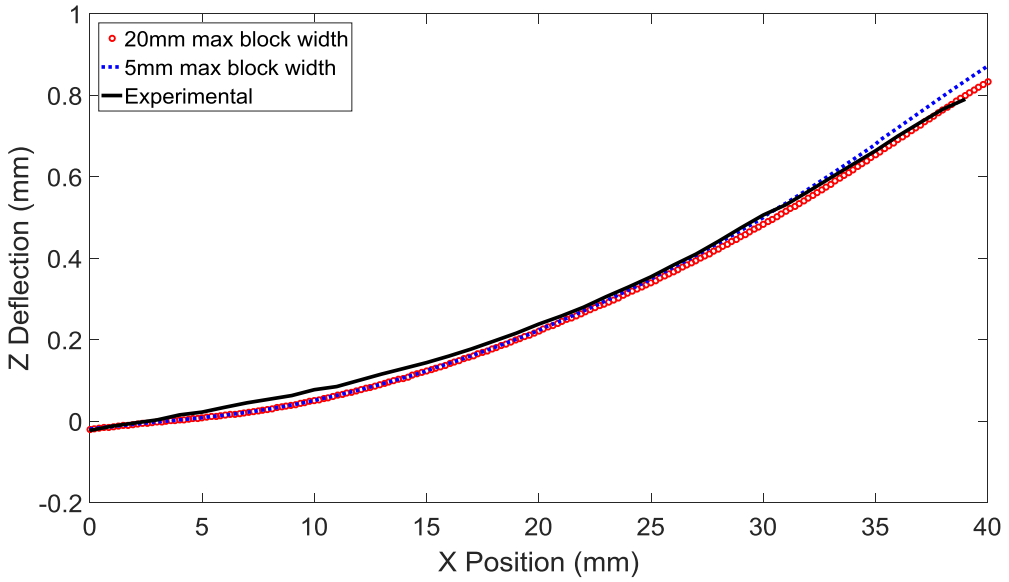

Figure 9: Plot showing the vertical deflection of the top surface about the centreline for two models of 0.83 mm block height and maximum (upper section) block widths of 5 mm and 20 mm.

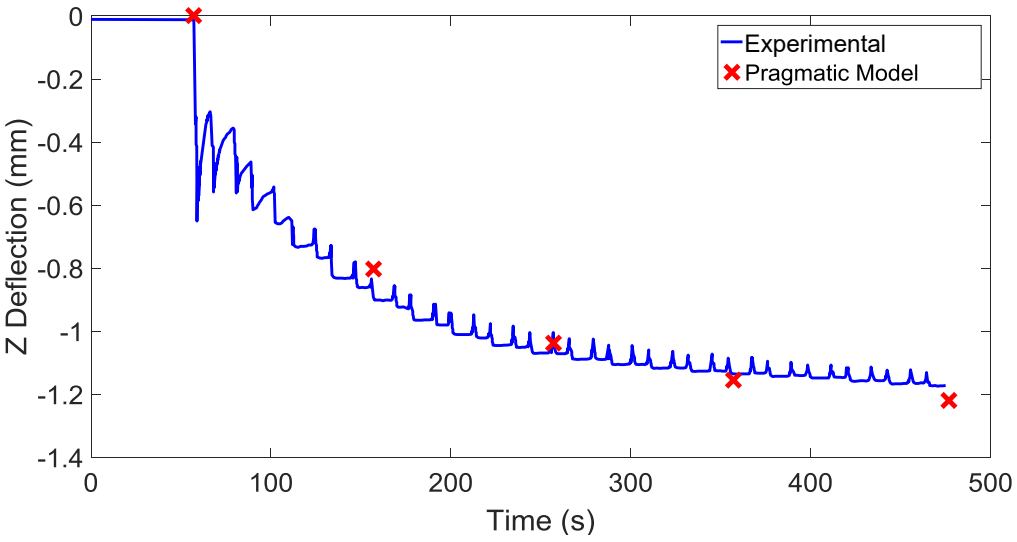

Figure 10: Plot comparing the vertical of the substrate through time, as predicted by the pragmatic model and measured experimentally by Dunbar et al. [21].

term response as the deflection approaches steady state. The final deflections measured by the LVDT and predicted by the pragmatic model were $-1.172\,\text{mm}$ and $-1.219\,\text{mm}$ respectively.

The principal stresses in the part are also compared with that of the model in [5]. Contour plots of the horizontal principal stress from both the pragmatic model and that of Denlinger et al. are shown in Figure 11. Similarities can be seen in terms of both the magnitude and the shape of the field. It can be seen that in both plots there is a region of high tensile stress near the surface of the part, surrounded by regions of tensile stress of a lower magnitude. In the centre of the part is a region of compressive stress. The maximum and minimum stress values predicted by the pragmatic model are within 10-20 % of those predicted by Denlinger et al. [5]. The additional fidelity of the more complex model can also be seen here with the stress fields corresponding to the individual scan lines traced out by the laser. This behaviour is not captured in the pragmatic model, though the magnitude and direction of the stresses are broadly similar.

7. Discussion

In the bridge component study a coarsened, or scaled, deposition strategy is adopted to reduce simulation time in PBF process modelling. Varying the number of blocks in the simulation revealed how much the strategy could be coarsened before the solutions diverged. The experimental bridge made from 316L had a layer height of $50\,\mu\text{m}$ and took a total of 200 layers to build. Results converged with modelling only 12 scaled layers, or a block height of $0.83\,\text{mm}$, giving a 16 times reduction in the number of analysis steps required and thus the simulation time. The converged solution is within 5% of the experimental measurements made via DIC. The thermal analysis took 100 minutes and the mechanical analysis took 12 hours wall clock time running on 12 CPUs. As a result of the reduced simulation time a larger component could be modelled and validated than can commonly be found in the literature.

Figures 7 and 8 also show the block deposition methodology converging in terms of both the vertical and horizontal sizes of the blocks. When a small number of coarse blocks are used the solution is less accurate but as fidelity is increased the prediction becomes very close to the experimental value. In reducing the vertical height of the blocks, the behaviour of the thermal model is tending towards what is happening in the physical process. The broader thermal process, particularly within the temperature range relevant to residual stress, is governed largely by the layer-by-layer vertical heating. The results suggest that for relatively small parts (with short scan times and simple topologies) that this pragmatic methodology sufficiently captures the thermal field present in the part and can accurately predict stress and distortion. In the case of a larger and more complex part topology, the block deposition strategy would require divisions in all 3 dimensions in order to approximate the thermal profile accurately. The result would also likely be more sensitive to the number of horizontal and through thickness block divisions. This may cause the model to become prohibitive in terms of setup complexity and simulation time.

The pragmatic model does not account for any effects of scan strategy. However at a coarse level the block divisions and activation sequence could follow the laser scanning strategy. For example a chessboard scan pattern could be replicated by activating each chessboard square or a group of squares sequentially. This may improve the accuracy in

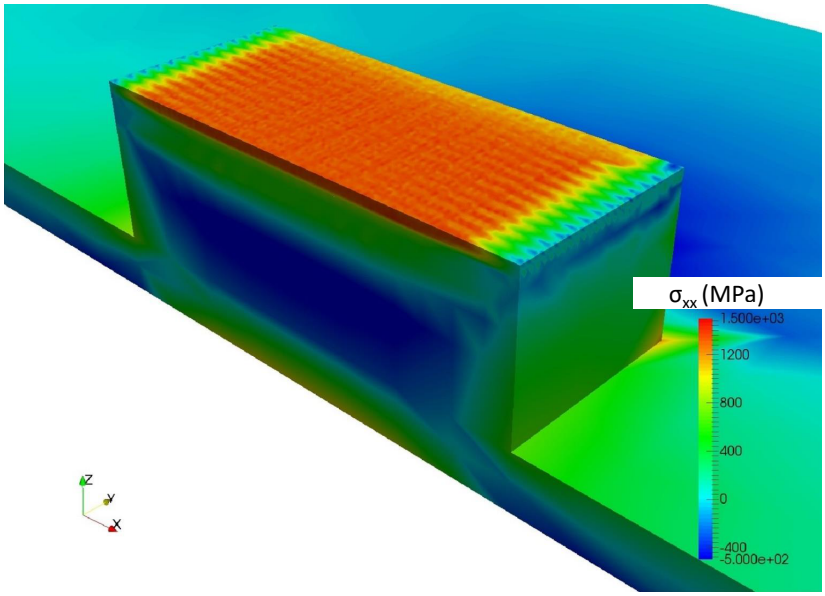

(a)

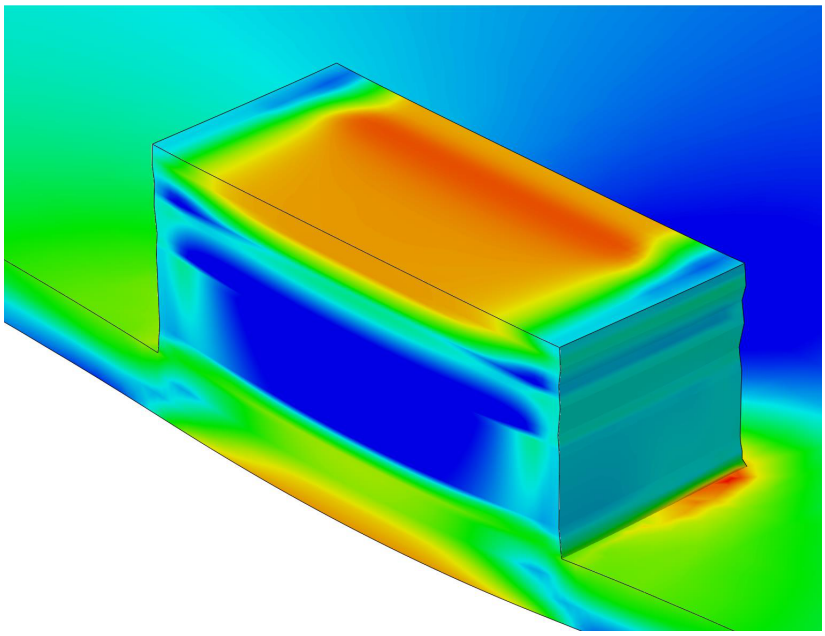

(b)

Figure 11: Section taken through the centre of the block showing the principal horizontal stress fields predicted at the final stage of the analysis from (a) the model of Denlinger et al. [5] and (b) the pragmatic model.

the net shape predicted as the temperature profile drives residual stress. This is also a more computationally efficient way of including scan strategy effects than by modelling the laser at its true spot diameter. Figure 9 shows small differences in the results when varying number of horizontal blocks used, indicating that this methodology may be suitable for investigating different scanning strategies.

The cuboid model of an Inconel 718 block on a thin substrate predicts the deflection to within 10% of the experimental measurement. The steady state deflection of the substrate converged after modelling 4 scaled blocks, compared to 38 layers in the experimental build. The simulation reached a solution in 30 minutes running on 4 cores. The principal stress fields within the part also matched well with those in the model presented by Denlinger et al. [5]. Although neither of these stress fields have been verified experimentally the stress fields predicted by both models are broadly characteristic of components manufactured by AM, which frequently exhibit high tensile residual stresses near the top surface. It can be inferred that they must be reasonably accurate quantitatively in order to predict the corresponding distortions. The results of this second verification model lend further weight to validity of this simplified methodology. They also demonstrate its applicability to a second material system and geometry.

Despite its coarse nature the pragmatic model proposed here successfully predicted the final distorted shape of two different parts. This indicates that it is approximating the thermal field sufficiently accurately in the temperature range that is relevant to residual stress development. That is, the model accurately captures the thermal field in this lower temperature range and the resulting mechanical deformation. It is for this reason that the model predictions remain accurate with a reduced number of simulation blocks.

8. Conclusion

In this study a thermomechanical FE model was presented which demonstrates the potential of applying a pragmatic methodology to residual stress and distortion prediction in PBF AM processes. The model was applied to two experimental problems in two different materials to compare the predicted net distortion with that measured experimentally. The predicted final distortions were within 10% of the experimental measurement with significant reduction in the computational effort required. The study has shown that it is not necessary to model every laser pass or even every deposited layer to accurately predict final part shape. The scaled deposition strategy and pragmatic approach to modelling presented here also yields results with comparable accuracy to more complex and computationally intensive models for both residual stress and distortion predictions. The approach allows process modelling of larger components to be conducted in a short and useful time frame. This makes it viable and advantageous for industry to integrate process modelling of PBF into their design and manufacturing systems.

9. Acknowledgements

We gratefully acknowledge AWE plc for funding Richard Williams' PhD and Paul Hooper's research fellowship.

10. References

[1] M. Grasso, B. M. Colosimo, Process defects and in situ monitoring methods in metal powder bed fusion: a review, Measurement Science and Technology 28 (4). doi:10.1088/1361-6501/aa5c4f.

[2] PwC Manufacturing Institute, 3D Printing comes of age in US industrial manufacturing (2016). URL `https://www.pwc.com/us/en/industrial-products/3d-printing-comes-of-age.html`

[3] M. Megahed, H.-W. Mindt, N. N'Dri, H. Duan, O. Desmaison, Metal additive-manufacturing process and residual stress modeling, Vol. 5, Integrating Materials and Manufacturing Innovation, 2016. doi:10.1186/s40192-016-0047-2.

[4] L. Parry, I. Ashcroft, R. Wildman, Understanding the effect of laser scan strategy on residual stress in selective laser melting through thermo-mechanical simulation, Additive Manufacturing 12 (2016) 1–15. doi:10.1016/j.addma.2016.05.014.

[5] E. R. Denlinger, M. Gouge, J. Irwin, P. Michaleris, Thermomechanical model development and in situ experimental validation of the laser powder-bed fusion process, Additive Manufacturing 16 (2017) 73–80. doi:10.1016/j.addma.2017.05.001.

[6] K. Dai, L. Shaw, Thermal and mechanical finite element modeling of laser forming from metal and ceramic powders, Acta Materialia 52 (1) (2004) 69–80.

[7] A. Hussein, L. Hao, C. Yan, R. Everson, Finite element simulation of the temperature and stress fields in single layers built without-support in selective laser melting, Materials & Design 52 (2013) 638–647. doi:10.1016/j.matdes.2013.05.070.

[8] C. H. Fu, Y. B. Guo, 3-Dimensional Finite Element Modeling of Selective Laser Melting Ti-6Al-4V Alloy, Solid Freeform Fabrication Symposium (2014) 1129–1144.

[9] W. King, A. T. Anderson, R. M. Ferencz, N. E. Hodge, C. Kamath, S. A. Khairallah, Overview of modelling and simulation of metal powder bed fusion process at Lawrence Livermore National Laboratory, Materials Science and Technology 31 (8) (2015) 957–968. doi:10.1179/1743284714Y.0000000728.

[10] M. Masoomi, S. M. Thompson, N. Shamsaei, A. Elwany, L. Bian, An Experimental-Numerical Investigation of Heat Transfer During Selective Laser Melting, Journal of Chemical Information and Modeling 53 (9) (2013) 1689–1699. arXiv:arXiv:1011.1669v3, doi:10.1017/CBO9781107415324.004.

[11] N. Contuzzi, S. L. Campanelli, A. D. Ludovico, 3D finite element analysis in the Selective Laser Melting process, International Journal of Simulation Modelling 10 (3) (2011) 113–121. doi:10.2507/IJSIMM10(3)1.169.

[12] I. A. Roberts, C. J. Wang, R. Esterlein, M. Stanford, D. J. Mynors, A three-dimensional finite element analysis of the temperature field during laser melting of metal powders in additive layer manufacturing, International Journal of Machine Tools and Manufacture 49 (12-13) (2009) 916–923. doi:10.1016/j.ijmachtools.2009.07.004.

[13] J. Goldak, A. Chakravarti, M. Bibby, A new finite element model for welding heat sources, Metallurgical Transactions B 15 (2) (1984) 299–305. doi:10.1007/BF02667333.

[14] K. Antony, N. Arivazhagan, K. Senthilkumaran, Numerical and experimental investigations on laser melting of stainless steel 316L metal powders, Journal of Manufacturing Processes 16 (3) (2014) 345–355. doi:10.1016/j.jmapro.2014.04.001.

[15] L. Ma, H. Bin, Temperature and stress analysis and simulation in fractal scanning-based laser sintering, The International Journal of Advanced Manufacturing Technology 34 (9-10) (2007) 898–903. doi:10.1007/s00170-006-0665-5.

[16] S. Marimuthu, D. Clark, J. Allen, a. M. Kamara, P. Mativenga, L. Li, R. Scudamore, Finite element modelling of substrate thermal distortion in direct laser additive manufacture of an aero-engine component, Proceedings of the Institution of Mechanical Engineers, Part C: Journal of Mechanical Engineering Science 227 (9) (2013) 1987–1999. doi:10.1177/0954406212470363.

[17] L.-E. Loh, C.-K. Chua, W.-Y. Yeong, J. Song, M. Mapar, S.-L. Sing, Z.-H. Liu, D.-Q. Zhang, Numerical investigation and an effective modelling on the Selective Laser Melting (SLM) process with aluminium alloy 6061, International Journal of Heat and Mass Transfer 80 (2015) 288–300. doi:10.1016/j.ijheatmasstransfer.2014.09.014.

[18] R. B. Patil, V. Yadava, Finite element analysis of temperature distribution in single metallic powder layer during metal laser sintering, International Journal of Machine Tools and Manufacture 47 (7-8) (2007) 1069–1080. doi:10.1016/j.ijmachtools.2006.09.025.

[19] N. E. Hodge, R. M. Ferencz, R. M. Vignes, Experimental comparison of residual stresses for a thermomechanical model for the simulation of selective laser melting, Additive Manufacturing 12 (2016) 159 – 168. doi:10.1016/j.addma.2016.05.011.

[20] J.-P. Kruth, J. Deckers, E. Yasa, R. Wauthlé, Assessing and comparing influencing factors of residual

stresses in selective laser melting using a novel analysis method, Proceedings of the Institution of Mechanical Engineers, Part B: Journal of Engineering Manufacture 226 (6) (2012) 980–991. doi:10.1177/0954405412437085.

[21] A. J. Dunbar, E. R. Denlinger, J. Heigel, P. Michaleris, P. Guerrier, R. Martukanitz, T. W. Simpson, Development of experimental method for in situ distortion and temperature measurements during the laser powder bed fusion additive manufacturing process, Additive Manufacturing 12. doi:10.1016/j.addma.2016.04.007.

[22] Dassault Systèmes, Abaqus 6.14 Documentation (2014).

[23] C. Truman, M. Smith, The net residual stress measurement and modelling round robin on a single weld bead-on-plate specimen, International Journal of Pressure Vessels and Piping 86 (1) (2009) 1–2. doi:10.1016/j.ijpvp.2008.11.018.

[24] C. Li, J. F. Liu, X. Y. Fang, Y. B. Guo, Efficient predictive model of part distortion and residual stress in selective laser melting, Additive Manufacturing 17 (2017) 157 – 168. doi:10.1016/j.addma.2017.08.014.

[25] L.-E. Lindgren, Computational welding mechanics: thermomechanical and microstructural simulations, Woodhead publishing in materials, Woodhead ; CRC Press, Cambridge : Boca Raton, Fla., 2007.

[26] B. Doyle, Optimisation and ductile damage evaluation of additively manufactured stainless steel 316L, Master's thesis, Imperial College London (2016).

[27] M. S. Pham, B. Dovgyy, P. A. Hooper, Twinning induced plasticity in austenitic stainless steel 316L made by additive manufacturing, Materials Science and Engineering: A 704 (2017) 102–111. doi:10.1016/j.msea.2017.07.082.

[28] C. Casavola, C. S.L., C. Pappalettere, Experimental analysis of residual stresses in the selective laser melting process, in: Society for Experimental Mechanics Inc. (Ed.), Proceedings of the XIth International Congress and Exposition, Orlando, 2008.

[29] G. R. Johnson, W. H. Cook, A Constitutive Model and Data for metals subjected to large strains, high strain rates and high temperatures, in: Proceedings of the 7th International Symposium on Ballistics, The Hague, 1983, pp. 541–547.

[30] R. Casati, J. Lemke, M. Vedani, Microstructure and Fracture Behavior of 316L Austenitic Stainless Steel Produced by Selective Laser Melting, Journal of Materials Science & Technology 32 (8) (2016) 738–744. doi:10.1016/j.jmst.2016.06.016.

[31] X. Shan, C. Davies, T. Wangsdan, N. O'Dowd, K. Nikbin, Thermo-mechanical modelling of a single-bead-on-plate weld using the finite element method, International Journal of Pressure Vessels and Piping 86 (1) (2009) 110–121. doi:10.1016/j.ijpvp.2008.11.005.

[32] Renishaw plc., Design for metal am - a beginner's guide (2017).
URL `http://www.renishaw.com/en/design-for-metal-am-a-beginners-guide-42652`

[33] A. S. Wu, D. W. Brown, M. Kumar, G. F. Gallegos, W. E. King, An Experimental Investigation into Additive Manufacturing-Induced Residual Stresses in 316L Stainless Steel, Metallurgical and Materials Transactions A 45 (13) (2014) 6260–6270. doi:10.1007/s11661-014-2549-x.